

An unsplit convolutional perfectly matched layer technique improved at grazing incidence for the viscoelastic wave equation

Roland Martin¹ and Dimitri Komatitsch^{1,2}

¹Université de Pau et des Pays de l'Adour, CNRS & INRIA Magique-3D, Laboratoire de Modélisation et d'Imagerie en Géosciences UMR 5212, Avenue de l'Université, 64013 Pau Cedex, France. E-mail: roland.martin@univ-pau.fr

²Institut universitaire de France, 103 boulevard Saint-Michel, 75005 Paris, France

Accepted 2009 May 27. Received 2009 April 16; in original form 2008 August 1

SUMMARY

In the context of the simulation of wave propagation, the perfectly matched layer (PML) absorbing boundary layer has proven to be efficient to absorb non-grazing incidence waves. However, the classical discrete PML cannot efficiently absorb waves reaching the absorbing layer at grazing incidence. This is observed, for instance, in the case of thin mesh slices, or in the case of sources located close to the absorbing boundaries or receivers located at large offset. In order to improve the PML efficiency at grazing incidence we derive an unsplit convolutional PML (CPML) for a fourth-order staggered finite-difference numerical scheme applied to the 3-D viscoelastic seismic wave equation. The time marching equations of the standard linear solid mechanisms used do not need to be split and only the memory variables associated with velocity derivatives are stored at each time step. This is important in the case of more than one damping mechanism. Memory storage is reduced by more than 70 per cent in the PML regions in 3-D simulations compared to split PMLs optimized at grazing incidence. We validate the technique based on a benchmark performed in a thin mesh slice.

Key words: Numerical solutions; Elasticity and inelasticity; Seismic attenuation; Computational seismology; Wave propagation.

1 INTRODUCTION

In the last 30 years, a variety of absorbing layer techniques have been developed in geophysics and particularly in seismic wave propagation modelling. They have been adapted to numerical techniques as different as finite differences, finite elements and spectral elements in order to reduce reflections at the outer boundaries of the computational domain and efficiently simulate unbounded media at the local or regional scale. Damping layers or 'sponge zones' (Cerjan *et al.* 1985; Sochacki *et al.* 1987), paraxial conditions (Clayton & Engquist 1977; Engquist & Majda 1977; Stacey 1988; Higdon 1991; Quarteroni *et al.* 1998), optimized conditions (Peng & Töksoz 1995), the eigenvalue decomposition method (Dong *et al.* 2005), continued fraction absorbing conditions (Guddati & Lim 2006), exact absorbing conditions on a spherical contour (Grote 2000) or asymptotic local or non-local operators (Givoli 1991; Hagstrom & Hariharan 1998) have been introduced. However, the local conditions generate spurious low frequency energy reflected back into the main domain at all angles of incidence, sponge layers require a prohibitive number of gridpoints to be relatively efficient, and paraxial conditions do not efficiently absorb waves reaching the boundaries at grazing incidence and can become unstable in some cases, for instance for a high value of Poisson's ratio.

As explained for instance in Komatitsch & Martin (2007) and Martin *et al.* (2008a), the perfectly matched layer (PML), intro-

duced by Bérenger (1994) for Maxwell's equations, avoids many (but not all) of these drawbacks. It has the advantage of having a null reflection coefficient at all angles of incidence and at all frequencies before discretization by a numerical scheme. It was rapidly reformulated in a split form with complex coordinate stretching (Chew & Weedon 1994; Collino & Monk 1998) and adapted to elastic (Chew & Liu 1996; Collino & Tsogka 2001; Komatitsch & Tromp 2003; Cohen & Fauqueux 2005; Festa & Vilotte 2005; Festa *et al.* 2005; Ma & Liu 2006; Drossaert & Giannopoulos 2007; Komatitsch & Martin 2007) and poroelastic media (Zeng *et al.* 2001; Martin *et al.* 2008a). Festa & Vilotte (2005) and Festa *et al.* (2005) improved the behaviour at grazing incidence in the elastic case by introducing a split form of the elastic wave equation with PML for a mixed displacement/velocity–stress spectral-element method and adding filtering in the PML to damp waves at grazing incidence. In Komatitsch & Martin (2007), we introduced a simpler unsplit version of such a convolutional PML (CPML) for the elastic case, and in Martin *et al.* (2008a) we extended it to the poroelastic case. This CPML technique has also been extended to heterogeneous anisotropic models in the presence of curved interfaces and a free surface using a high-order finite-element method (Martin *et al.* 2008b). Besides the ease of implementation of such an unsplit method, it also allows one to reduce memory storage in the PML regions. In this paper, we extend our unsplit finite-difference formulation to the viscoelastic wave equation and discuss its efficiency.

The method is implemented using a fourth-order finite-difference scheme in space based on an unsplit formulation that involves a Butterworth filter and convolutional memory variables, as in the elastic case. The main advantage of this CPML formulation over split PML formulations such as the generalized frequency-dependent PML (GFPML) of Festa & Vilotte (2005) lies in the drastic reduction of memory storage in the PML regions and easier implementation because the different fields (velocities, stresses and all the attenuation mechanisms) do not need to be split for each spatial coordinate, nor do the auxiliary memory variables that are needed in the GFPML. Only the derivatives of the stresses and velocities need to be computed at each time step, which allows one to advance the attenuation memory variables in time without splitting each attenuation mechanism and therefore drastically reduce memory storage in the PML regions. It is important to notice that in the classical PML or in split optimized versions such as the GFPML the number of split variables increases with the number of viscoelastic standard linear solid (SLS) damping mechanisms, while the number of auxiliary variables remains the same in our CPML.

2 PHYSICAL PROBLEM UNDER STUDY

The displacement field \mathbf{u} produced by a seismic source is governed by the momentum equation

$$\rho \partial_t^2 \mathbf{u} = \nabla \cdot \mathbf{T} + \mathbf{f}. \quad (1)$$

The seismic source is represented by the point force \mathbf{f} , which may be written as

$$\mathbf{f} = -\delta(\mathbf{x} - \mathbf{x}_s) S(t). \quad (2)$$

The location of the point source is denoted by \mathbf{x}_s , $\delta(\mathbf{x} - \mathbf{x}_s)$ denotes the Dirac delta distribution located at \mathbf{x}_s , and the source time function is given by $S(t)$. The distribution of density is denoted by ρ . The stress tensor \mathbf{T} is linearly related to the displacement gradient $\nabla \mathbf{u}$ by Hooke's law, which in a pure elastic solid may be written in the form

$$\mathbf{T} = \mathbf{c} : \nabla \mathbf{u}, \quad (3)$$

the elastic properties being determined by the fourth-order elastic tensor \mathbf{c} . In an attenuating medium, Hooke's law (3) is modified such that the stress is determined by the entire strain history

$$\mathbf{T}(t) = \int_{-\infty}^{\infty} \partial_t \mathbf{c}(t - \tau) : \nabla \mathbf{u}(\tau) d\tau. \quad (4)$$

The viscoelastic properties of a medium can be modelled in the time domain in different ways using a series of SLS mechanisms (Liu *et al.* 1976), for instance using the rheological model of a generalized Zener body (Carcione 2007) or a generalized Maxwell body (Emmerich & Korn 1987). According to Moczo & Kristek (2005) these two rheological models are equivalent and we therefore decided to use the Zener body model. In seismic wave propagation modelling the quality factor Q can often be considered constant over a wide frequency band and modelled as a series of L SLS mechanisms, with $L = 3$ commonly used to mimic an almost constant Q (Emmerich & Korn 1987). In the absorption band the components of the anelastic tensor for such a series can be expressed in terms of the relaxed modulus c_{ijkl}^R and the unrelaxed components c_{ijkl}^U , which are related by

$$c_{ijkl}^U = c_{ijkl}^R \left[1 - \sum_{\ell=1}^L \left(1 - \tau_{ijkl}^{\epsilon\ell} / \tau^{\sigma\ell} \right) \right]. \quad (5)$$

A stress relaxation time $\tau^{\sigma\ell}$ and a strain relaxation time $\tau_{ijkl}^{\epsilon\ell}$ are defined for each component and the modulus defect $\delta\mathbf{c}^\ell$ associated with each SLS is determined by

$$\delta c_{ijkl}^{\epsilon\ell} = -c_{ijkl}^R \left(1 - \tau_{ijkl}^{\epsilon\ell} / \tau^{\sigma\ell} \right). \quad (6)$$

The constitutive relation (4) may then be rewritten in the form (see e.g. Komatitsch & Tromp 1999)

$$\mathbf{T} = \mathbf{c}^U : \nabla \mathbf{u} - \sum_{\ell=1}^L \mathbf{R}^\ell, \quad (7)$$

where for each SLS

$$\partial_t \mathbf{R}^\ell = -\mathbf{R}^\ell / \tau^{\sigma\ell} + \delta\mathbf{c}^\ell : \nabla \mathbf{u} / \tau^{\sigma\ell}. \quad (8)$$

For more details, the reader is referred for instance to Komatitsch & Tromp (1999) and Moczo *et al.* (2007). In the classical first-order velocity–stress formulation, one first rewrites eqs (1), (7) and (8) as

$$\begin{aligned} \rho \partial_t \mathbf{v} &= \nabla \cdot \mathbf{T} \\ \partial_t \mathbf{T} &= \mathbf{c}^U : \nabla \mathbf{v} - \sum_{\ell=1}^L \mathbf{R}^\ell \\ \partial_t \mathbf{R}^\ell &= -\mathbf{R}^\ell / \tau^{\sigma\ell} + \delta\mathbf{c}^\ell : \nabla \mathbf{v} / \tau^{\sigma\ell}, \end{aligned} \quad (9)$$

where \mathbf{v} is the velocity vector. Bold notations indicate a tensor and italics notations with sub-indices indicate a tensor component. We can introduce the expression of the strain rate tensor $\boldsymbol{\epsilon}$

$$\epsilon_{ij} = \frac{1}{2} \left(\frac{\partial v_i}{\partial x_j} + \frac{\partial v_j}{\partial x_i} \right), \quad (10)$$

where indices i and j can be 1, 2 or 3 in 3-D, and the trace of the strain-rate tensor $\text{Tr}(\boldsymbol{\epsilon}) = \sum_{i=1}^D \epsilon_{ii}$ where $D = 3$ is the spatial dimension of the problem and rewrite the system as

$$\begin{aligned} \rho \partial_t v_i &= \partial_j T_{ij} \\ \partial_t T_{ij} &= \lambda^U \delta_{ij} \text{Tr}(\boldsymbol{\epsilon}) + 2\mu^U \epsilon_{ij} - \sum_{\ell=1}^L R_{ij}^\ell \\ \partial_t R_{ij}^\ell &= -R_{ij}^\ell / \tau^{\sigma\ell} + \delta c_{ik}^{\epsilon\ell} \epsilon_{kj} / \tau^{\sigma\ell}. \end{aligned} \quad (11)$$

The frequency-domain form of this system is then

$$\begin{aligned} i\omega \rho v_i &= \partial_j T_{ij} \\ i\omega T_{ij} &= \lambda^U \delta_{ij} \text{Tr}(\boldsymbol{\epsilon}) + 2\mu^U \epsilon_{ij} - \sum_{\ell=1}^L R_{ij}^\ell \\ i\omega R_{ij}^\ell &= -R_{ij}^\ell / \tau^{\sigma\ell} + \delta c_{ik}^{\epsilon\ell} \epsilon_{kj} / \tau^{\sigma\ell}, \end{aligned} \quad (12)$$

where $\omega = 2\pi f$ denotes angular frequency and where for simplicity we have used the same notation for the fields in the time and frequency domains.

3 THE CLASSICAL PML AND CPML FORMULATIONS

The main idea behind the PML technique consists in reformulating the derivatives in directions x , y and z in the six layers surrounding the physical domain. In practice, eq. (12) is solved based on the system of equations of the Appendix. The mechanisms \mathbf{R}^ℓ are combinations of elemental mechanisms \mathbf{E}^ℓ , the relaxed parameters λ^R and μ^R and the relaxation times of the different mechanisms, whose expressions are given in the Appendix according to the model defined by Carcione (1993).

3.1 The classical PML in velocity–stress formulation

As for instance in Gedney (1998) and Collino & Tsogka (2001), a damping profile $d_x(x)$ is defined in the PML region such that $d_x = 0$ inside the main domain and $d_x > 0$ in the PML, and a new complex coordinate \tilde{x} is expressed as

$$\tilde{x}(x) = x - \frac{i}{\omega} \int_0^x d_x(s) ds. \quad (13)$$

In directions y and z , similar damping profiles $d_y(y)$ and $d_z(z)$ are defined. Using the fact that

$$\partial_{\tilde{x}} = \frac{i\omega}{i\omega + d_x} \partial_x = \frac{1}{s_x} \partial_x, \quad (14)$$

with

$$s_x = \frac{i\omega + d_x}{i\omega} = 1 + \frac{d_x}{i\omega}, \quad (15)$$

and deriving a similar expression of $\partial_{\tilde{y}}$, $\partial_{\tilde{z}}$, s_y and s_z , one replaces all x derivatives ∂_x , y derivatives ∂_y and z derivatives ∂_z with \tilde{x} derivatives $\partial_{\tilde{x}}$, \tilde{y} derivatives $\partial_{\tilde{y}}$ and \tilde{z} derivatives $\partial_{\tilde{z}}$, respectively. One then uses the mapping (14) to rewrite eq. (12) in terms of x , y and z rather than \tilde{x} , \tilde{y} and \tilde{z}

$$\begin{aligned} i\omega \rho v_i &= \frac{1}{s_j} \partial_i T_{ij} \\ i\omega T_{ij} &= \lambda^U \frac{1}{s_k} \partial_k v_k \delta_{ij} + \mu^U \left(\frac{1}{s_i} \partial_i v_i + \frac{1}{s_j} \partial_j v_j \right) - \sum_{\ell=1}^L R_{ij}^{\ell} \\ i\omega R_{ij}^{\ell} &= -R_{ij}^{\ell} / \tau^{\sigma\ell} + \delta c_{im}^{\ell} \frac{1}{2} (\partial_m v_j + \partial_j v_m) / \tau^{\sigma\ell}, \end{aligned} \quad (16)$$

where indices i, j and m can be 1, 2 or 3 (equivalently x, y or z) in 3-D. One subsequently splits the velocity and stress fields and attenuation mechanisms into three components such that $\mathbf{v} = \mathbf{v}^1 + \mathbf{v}^2 + \mathbf{v}^3$, $\mathbf{T} = \mathbf{T}^1 + \mathbf{T}^2 + \mathbf{T}^3$ and $\mathbf{R}^{\ell} = \mathbf{R}^{\ell 1} + \mathbf{R}^{\ell 2} + \mathbf{R}^{\ell 3}$ and eq. (16) writes as follows:

$$\begin{aligned} i\omega \rho v_i^k &= \frac{1}{s_k} \partial_k T_{ik}, \quad k = 1, 2, 3 \text{ (or equivalently } x, y, z), \quad i = 1, 2, 3 \\ i\omega T_{ij}^k &= \lambda^U \frac{1}{s_k} \partial_k v_k \delta_{ij} + \mu^U \left(\delta_{ik} \frac{1}{s_i} \partial_i v^j + \delta_{jk} \frac{1}{s_j} \partial_j v^i \right) - \sum_{\ell=1}^L R_{ij}^{\ell k} \\ i\omega R_{ij}^{\ell k} &= -R_{ij}^{\ell k} / \tau^{\sigma\ell} + \delta c_{im}^{\ell} \frac{1}{2} \left(\delta_{mk} \frac{1}{s_m} \partial_m v^j + \delta_{jk} \frac{1}{s_j} \partial_j v^m \right) / \tau^{\sigma\ell} \\ v_i &= \sum_{k=1}^3 v_i^k, \quad i = x, y, z \\ T_{ii} &= \sum_{k=1}^3 T_{ii}^k, \quad i = x, y, z \\ T_{ij} &= T_{ij}^i + T_{ij}^j, \quad i \neq j \text{ and } i, j = x, y, z \\ R_{ii}^{\ell} &= \sum_{k=1}^3 R_{ii}^{\ell k}, \quad i = x, y, z \\ R_{ij}^{\ell} &= R_{ij}^{\ell i} + R_{ij}^{\ell j}, \quad i \neq j \text{ and } i, j = x, y, z. \end{aligned} \quad (17)$$

Using an inverse Fourier transform one goes back to the time domain and obtains the classical PML formulation of the viscoelastic

equations written in a split form

$$\begin{aligned} (\partial_t + d_k) \rho v_i^k &= \partial_k T_{ik}, \quad k = 1, 2, 3 \text{ (or equivalently } x, y, z), \\ & \quad i = 1, 2, 3 \\ (\partial_t + d_k) T_{ij}^k &= \lambda^U \partial_k v_k \delta_{ij} + \mu^U (\delta_{ik} \partial_i v^j + \delta_{jk} \partial_j v^i) \\ & \quad - \sum_{\ell=1}^L \left(R_{ij}^{\ell k} + d_k \int_{-\infty}^t R_{ij}^{\ell k} d\tau \right) \\ (\partial_t + d_k) R_{ij}^{\ell k} &= -R_{ij}^{\ell k} / \tau^{\sigma\ell} + \delta c_{im}^{\ell} \frac{1}{2} (\delta_{mk} \partial_m v^j + \delta_{jk} \partial_j v^m) / \tau^{\sigma\ell} \\ v_i &= \sum_{k=1}^3 v_i^k, \quad i = x, y, z \\ T_{ii} &= \sum_{k=1}^3 T_{ii}^k, \quad i = x, y, z \\ T_{ij} &= T_{ij}^i + T_{ij}^j, \quad i \neq j \text{ and } i, j = x, y, z \\ R_{ii}^{\ell} &= \sum_{k=1}^3 R_{ii}^{\ell k}, \quad i = x, y, z \\ R_{ij}^{\ell} &= R_{ij}^{\ell i} + R_{ij}^{\ell j}, \quad i \neq j \text{ and } i, j = x, y, z. \end{aligned} \quad (18)$$

Unfortunately, as we will show in the section about numerical tests below, this classical PML formulation is not very efficient after numerical discretization for waves reaching the absorbing layer at grazing incidence. Therefore, let us introduce an unsplit CPML technique improved at grazing incidence for viscoelastic media.

3.2 The unsplit CPML technique improved at grazing incidence for viscoelastic media

Let us summarize the CPML technique developed in the elastic case by Komatitsch & Martin (2007) and in the poroelastic case by Martin *et al.* (2008a) and let us extend it to the velocity–stress formulation of the viscoelastic wave equation. The key idea of the CPML lies in using a more general choice for s_x than that of eq. (14) by introducing the real variables $\alpha_x \geq 0$ and $\kappa_x \geq 1$ such that

$$s_x = \kappa_x + \frac{d_x}{\alpha_x + i\omega}. \quad (19)$$

In the case of an attenuating medium, the wavenumber is complex and therefore waves are further damped with the additional exponential factor $e^{-\text{Im}(k_x) \kappa_x x}$ inside the PML region, where $\text{Im}(k_x)$ is the imaginary part of the wave number. Therefore, the waves are damped further when κ_x increases in the CPML layer from 1 at its base to a maximum value κ_{\max} at its top. However, as described in the next section, from a numerical point of view κ_x cannot be increased too drastically because the reflection coefficient of waves impinging on the boundary would increase because of the staircase discretization of sharp variations of the profile of the κ_x function. Therefore, at low frequencies (and therefore long time periods), waves are more attenuated, while at high frequencies the CPML behaves very similarly to the classical PML.

Denoting by $\bar{s}_x(t)$ the inverse Fourier transform of $\frac{1}{s_x}$, ∂_x is replaced with

$$\partial_x = \bar{s}_x(t) * \partial_x. \quad (20)$$

After calculating the expression of $\bar{s}_x(t)$ and after some algebraic operations [see eqs (17) and (18) in Komatitsch & Martin (2007)],

we obtain

$$\partial_x = \frac{1}{\kappa_x} \partial_x + \zeta_x(t) * \partial_x. \tag{21}$$

with

$$\zeta_x(t) = -\frac{d_x}{\kappa_x^2} H(t) e^{-(d_x/\kappa_x + \alpha_x)t}, \tag{22}$$

where H is the Heaviside distribution. As we have null initial conditions, the convolution term at time step n can be approximated following the recursive convolution method of Luebbers & Hunsberger (1992):

$$\psi_x^n = (\zeta_x * \partial_x)^n \simeq \sum_{m=0}^{N-1} Z_x(m) (\partial_x)^{n-(m+1/2)} \tag{23}$$

with

$$Z_x(m) = -\frac{d_x}{\kappa_x^2} \int_{m\Delta t}^{(m+1)\Delta t} e^{-(d_x/\kappa_x + \alpha_x)\tau} d\tau = a_x e^{-(d_x/\kappa_x + \alpha_x)m\Delta t}. \tag{24}$$

Setting

$$b_x = e^{-(d_x/\kappa_x + \alpha_x)\Delta t} \quad \text{and} \quad a_x = \frac{d_x}{\kappa_x(d_x + \kappa_x\alpha_x)}(b_x - 1) \tag{25}$$

and developing $Z(x)$ in eq. (23), the convolution term can be viewed as a recursive sum. Therefore, we can update the memory variable ψ_x of the derivative of variable f (velocity or stress) along direction x at each time step based on

$$\psi_x^n(f) = b_x \psi_x^{n-1}(f) + a_x (\partial_x f)^{n-1/2}. \tag{26}$$

This formulation can be easily implemented in an existing finite-difference code without PML by simply replacing the spatial derivatives ∂_x with $\frac{1}{\kappa_x} \partial_x + \psi_x$ and advancing ψ_x in time using the same time evolution scheme as for the other (existing) variables.

The memory storage needed to implement CPML for the viscoelastic wave equation for one damping mechanism is similar to the first-order velocity–stress formulation of the more classical PML, as can be seen in Table 1 which gives the number of arrays inside each PML layer. However in the case of more than one damping mechanism the CPML is more advantageous because time-evolution equations of damping mechanisms do not need to be split and only the space derivatives of velocities need to be stored at each time step, as is the case for the calculation of velocities. On the contrary, for split PMLs or the GFPML all the solid mechanism equations need to be split along the three directions, which is expensive in terms of memory storage in the PML regions.

Table 1. Maximum number of arrays needed in the PML regions to implement a 3-D elastic or viscoelastic rheology for the classical PML technique without storing the total field, that is, the sum of the split components, which is then recomputed in each loop; the optimized split GFPML; and the classical PML technique, storing the total field; and the CPML technique. This maximum number is reached in regions in which all the PML layers are present, that is, in the corners of the domain. For comparison, we also recall the number of arrays needed when no absorbing conditions are implemented in the finite-difference technique.

	No PML	PML No total	PML With total	GFPML	CPML
Elastic	9	24	33	48	19
Viscoelastic	21	84	111	168	39

Furthermore, the classical PML requires an extra memory variable to handle the dissipative term that is not present in the CPML formulation, the CPML being essentially based upon the complex change of variable for first derivative calculations independently of the presence or absence of dissipative terms. The CPML technique requires 39 arrays in 3-D while the classical PML requires 111 arrays in 3-D, which means a gain of 64 per cent in the PML regions, and the optimized GFPML requires 168 arrays in 3-D, that is, the gain is then 76 per cent in the PML regions. If we denote by α the number of arrays inside the computational domain without PML and β the number of arrays inside the six PML regions the ratio of memory storage in the PML versus memory storage in the whole computational domain is

$$\frac{2\alpha N_{\text{pml}}(NX * NY + NY * NZ + NX * NZ)}{\beta * NX * NY * NZ} = \frac{2\alpha N_{\text{pml}}}{\beta} \left(\frac{1}{NX} + \frac{1}{NY} + \frac{1}{NZ} \right). \tag{27}$$

As $\beta = 21$, $\alpha = 39$ and $N_{\text{pml}} = 10$ in this study, we obtain a memory storage ratio of about $37(\frac{1}{NX} + \frac{1}{NY} + \frac{1}{NZ})$.

4 NUMERICAL TESTS

4.1 Model and test description

We consider simulations in 3-D for thin slices surrounded by CPML layers of a thickness of 10 gridpoints each. The size of each grid cell is $\Delta x = \Delta y = \Delta z = 3.5$ m. The medium is heterogeneous and consists of two layers with a flat interface. The upper layer has a relaxed pressure wave speed $c_p^R = 3000$ m s⁻¹, a shear wave speed $c_s^R = 2000$ m s⁻¹ and a density $\rho = 2000$ kg m⁻³ and the lower part has a relaxed pressure wave speed $c_p^R = 2500$ m s⁻¹, a shear wave speed $c_s^R = 1450$ m s⁻¹ and a density $\rho = 1500$ kg m⁻³. All the attenuation mechanisms are taken from Carcione *et al.* (1988). They correspond to very strong attenuation with constant quality factors $Q_p \simeq 30$ and $Q_s \simeq 20$. The values of the relaxation times are $\tau_{\epsilon 1}^1 = 0.03253$, $\tau_{\sigma 1}^1 = 0.031146$, $\tau_{\epsilon 1}^2 = 0.033257$, $\tau_{\sigma 1}^2 = 0.030465$, $\tau_{\epsilon 2}^1 = 0.003253$, $\tau_{\sigma 2}^1 = 0.003114$, $\tau_{\epsilon 2}^2 = 0.003325$ and $\tau_{\sigma 2}^2 = 0.003046$.

We use a slice of 735 m × 2800 m × 770 m surrounded by six CPML layers. The interface is located in the middle of the model at $y = 1400$ m. The grid (including the CPML layers) has a total size of 210 × 800 × 220 = 37 million gridpoints. The time step Δt of our explicit time scheme must obey the Courant–Friedrichs–Lewy (Courant *et al.* 1928) stability condition

$$\text{CFL} = \max \left(c_p^U \Delta t \sqrt{\frac{1}{\Delta x^2} + \frac{1}{\Delta y^2} + \frac{1}{\Delta z^2}} \right) \leq \text{CFL}_{\text{max}}, \tag{28}$$

where c_p^U is the pressure velocity of the unrelaxed material, equal to 3249 m s⁻¹ in the upper layer as in Carcione (1993) and to 2707 m s⁻¹ in the lower layer. We select a time step $\Delta t = 0.35$ ms (i.e. a CFL number equal to 0.54, slightly below the maximum value $\text{CFL}_{\text{max}} = 1/\sqrt{D} \simeq 0.577$). The simulation is performed for 100 000 time steps, that is, for a total duration of 35 s. The source is a force tilted at 45° and located at point ($x_s = 55$ m, $y_s = 560$ m and $z_s = 385$ m) close to the left CPML layer, at 20 gridpoints from its base, in order to generate pressure and shear waves impinging the CPML layers at different angles of incidence. The time variation of the source is a Ricker wavelet (i.e. the second derivative of a Gaussian) with a dominant frequency $f_0 = 18$ Hz, shifted in time by $t_0 = 1.2/f_0 = 0.066$ s in order to have null initial

conditions. The size of the mesh being too large to be run on a single processor, we implement the finite-difference algorithm on a parallel computer with hybrid message-passing (MPI) and shared-memory (OpenMP) programming using IEEE double precision in order to be able to compute small residuals of total energy accurately in the next sections.

Following Gedney (1998) and Collino & Tsogka (2001), the damping profile in the PML is chosen as $d_x(x) = d_0(\frac{x}{L})^N$ along

the x axis, $d_y(y) = d_0(\frac{y}{L})^N$ along the y -axis and $d_z(z) = d_0(\frac{z}{L})^N$ along the z -axis where L is the thickness of the absorbing layer, $N = 2$ and $d_0 = -\frac{(N+1)c_p^{U_{\max}} \log(R_c)}{2L} \simeq 1147.5$, $c_p^{U_{\max}}$ being equal to the maximum unrelaxed speed of the pressure wave and R_c being the target theoretical reflection coefficient, set to 0.1 per cent here. As in Roden & Gedney (2000), we make α_x , α_y and α_z vary linearly in the PML layer between a maximum value α_{\max} at the beginning of the PML and zero at the top. As in Festa & Vilotte (2005),

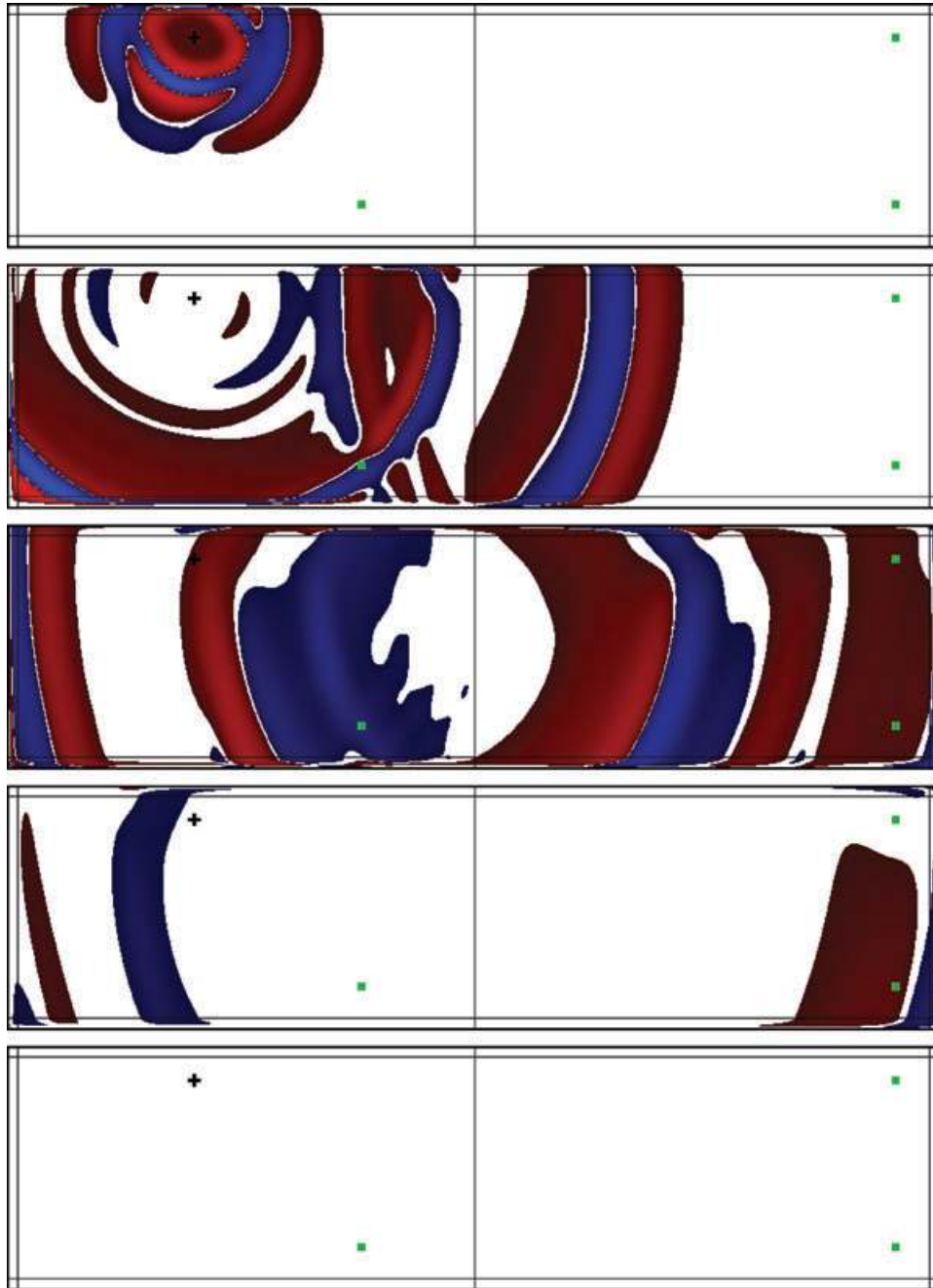


Figure 1. Snapshots of the v_y component of the 3-D velocity vector in a 2-D cutplane located in the middle of the grid along the z -axis for a viscoelastic medium corresponding to a thin slice with CPML conditions with $\alpha_{\max} = \pi f_0$ and $\kappa_{\max} = 1$ implemented on its six sides, at time 0.175 s (top panel), 0.525, 0.875, 1.225 and 1.575 s (bottom panel). We represent it in red (positive) or blue (negative) when it has an amplitude higher than a threshold of 1 per cent of the maximum, and the normalized value is raised to the power 0.30 to enhance small amplitudes that would otherwise not be clearly visible. The black cross indicates the location of the source and the green squares the position of receivers at which seismograms represented in the left-hand column of Figs 3–5 are recorded. The four vertical or horizontal black lines represent the edge of each PML layer. The black line dividing the medium represents the interface between the two media. No spurious wave of significant amplitude is visible, even at grazing incidence. The snapshots have been rotated by 90° to fit on the page.

we take $\alpha_{\max} = \pi f_0$, where f_0 is the dominant frequency of the source defined above, and we compare the results with $\alpha_{\max} = 0$ and $\kappa = 1$ which is very similar to the classical PML case of Collino & Tsogka (2001) because the Butterworth filter is then suppressed, as mentioned in Komatitsch & Martin (2007). We make κ_x , κ_y and κ_z vary from 1 at the base of the PML to a value κ_{\max} at the top of

the CPML with a polynomial variation of degree $N = 2$

$$\kappa_{x_i} = 1 + (\kappa_{\max} - 1) \left(\frac{x_i}{L} \right)^N, \quad x_i = x, y, z. \quad (29)$$

A series of simulations is performed with different values of κ_{\max} : 1, 7 and 20. On the external edges of the grid, that is, at the top of

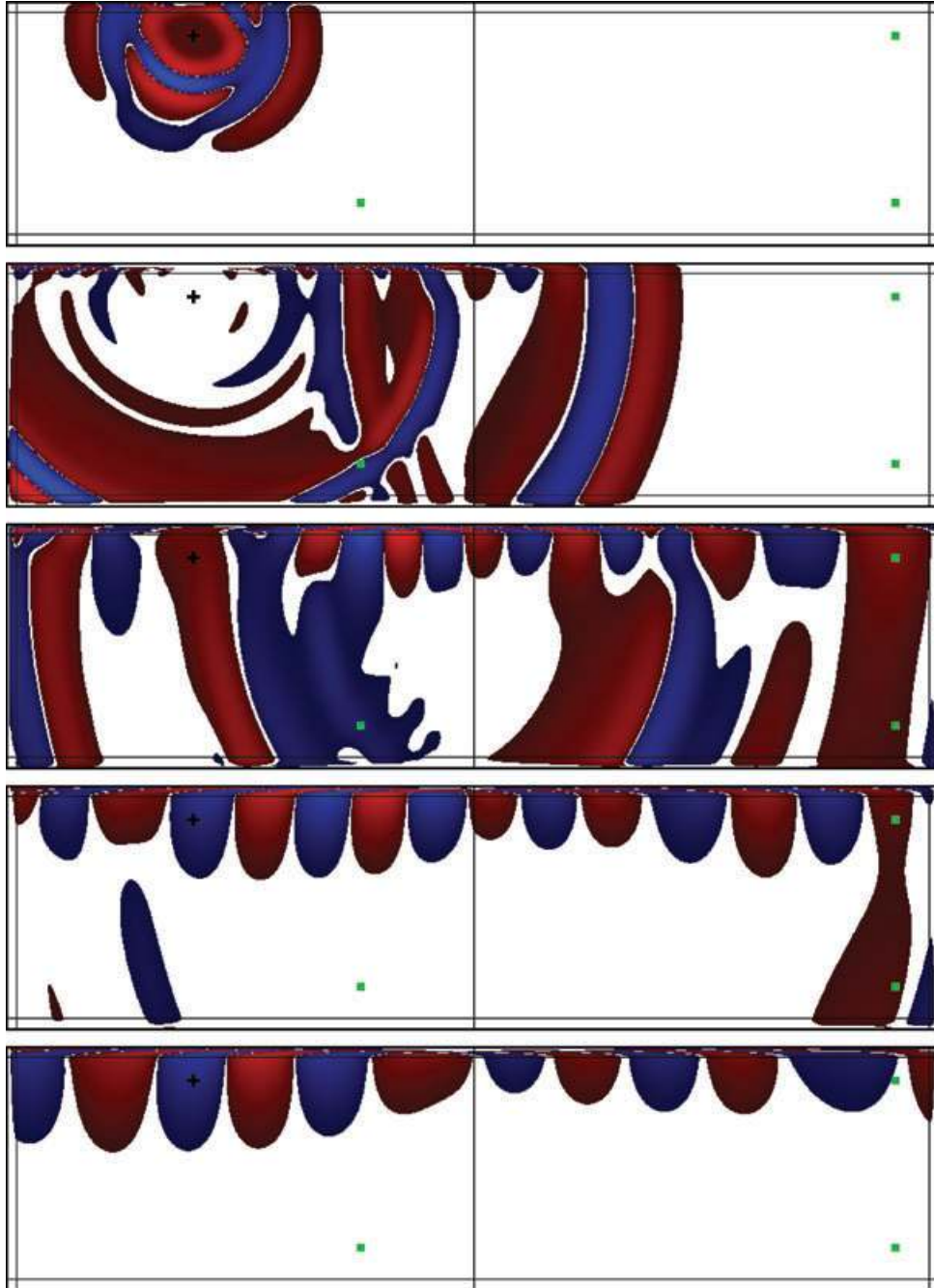


Figure 2. Snapshots of the v_y component of the 3-D velocity vector in a 2-D cutplane located in the middle of the grid along the z axis for a viscoelastic medium corresponding to a thin slice with CPML conditions with $\alpha_{\max} = 0$ and $\kappa_{\max} = 1$ implemented on its six sides, at time 0.175 s (top panel), 0.525, 0.875, 1.225 and 1.575 s (bottom panel). We represent it in red (positive) or blue (negative) when it has an amplitude higher than a threshold of 1 per cent of the maximum, and the normalized value is raised to the power 0.30 to enhance small amplitudes that would otherwise not be clearly visible. The black cross indicates the location of the source and the green squares represent the position of receivers at which seismograms represented in the right-hand column of Figs 3–5 are recorded. The four vertical or horizontal black lines represent the edge of each PML layer. The black line dividing the medium represents the interface between the two media. Compared to Fig. 1, spurious waves appear at grazing incidence along the edges of the model and send spurious energy back into the main domain. The snapshots have been rotated by 90° to fit on the page.

each PML, we impose a Dirichlet condition on the velocity vector ($\mathbf{v} = \mathbf{0}$ for all t). The vertical component of the velocity vector is recorded at three receivers located close to the edges of the grid in the XY plane located at $NZ/2$, in $(x_1 = 555 \text{ m}, y_1 = 1060 \text{ m}$ and $z_1 = 385 \text{ m})$, $(x_2 = 55 \text{ m}, y_2 = 2660 \text{ m}$ and $z_2 = 385 \text{ m})$ and $(x_3 = 555 \text{ m}, y_3 = 2660 \text{ m}$ and $z_3 = 385 \text{ m})$ in order to analyse the effects of the boundary conditions on waves propagating at grazing incidence.

4.2 Shifted and non-shifted CPML

Let us compare the efficiency of CPML with shifting of the poles to CPML without shifting. Fig. 1 shows snapshots of shifted CPML with $\alpha_{\max} = \pi f_0$ and $\kappa_{\max} = 1$ at different times. Waves propagate in all directions and undergo reflection and transmission at the interface between the two media. The snapshots do not exhibit significant spurious oscillations, even at grazing incidence, while non-physical spurious oscillations arise in the case of the non-shifted CPML with $\alpha_{\max} = 0$ (Fig. 2). As we will now see, these oscillations coming mainly from the left PML layer because of the position of the source are drastically attenuated for all values of κ_{\max} in the shifted case while they are gradually attenuated in the non-shifted case when κ_{\max} is increased from 1 to 20, although still remaining important in the case of $\alpha_{\max} = 0$ for $\kappa_{\max} = 20$.

To get more insight on the accuracy of both methods, in Figs 3–5, we show comparisons between shifted or non-shifted CPMLs and a reference solution computed with the same numerical scheme on a very large grid with no absorbing boundary conditions. Shifted and non-shifted CPMLs are tested with $\kappa_{\max} = 1, 7$ or 20. For all these values the error is small in both the shifted and non-shifted cases at point (x_1, y_1) (Fig. 3). Only comparisons for $\kappa_{\max} = 1$ are shown here because the results are extremely similar for $\kappa_{\max} = 7$ and 20.

On the contrary the solution with non-shifted CPML is significantly distorted at point (x_2, y_2) (Fig. 4) for $\kappa_{\max} = 1$ or 7 while the solution is much more accurate in the shifted case. However, if $\kappa_{\max} = 20$ the calculated waveform is much more accurate in both cases although some slight discrepancies and small errors in the amplitude are still present in the non-shifted case. At point (x_3, y_3) (Fig. 5) solutions are very similar in both the shifted and non-shifted cases and for all values κ_{\max} and fit the reference solution very well.

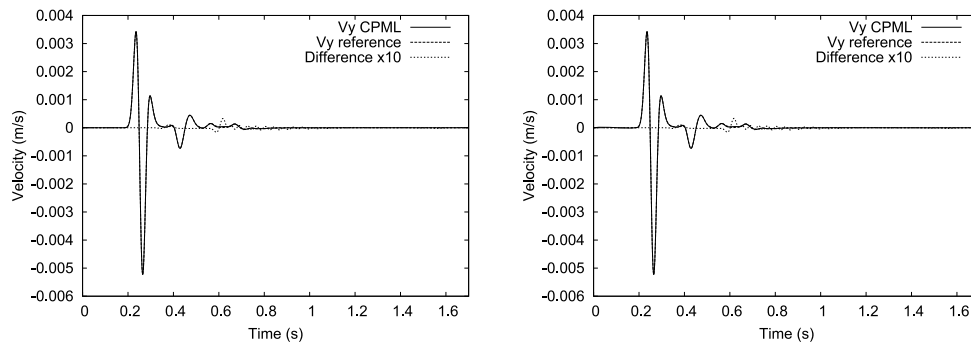


Figure 3. Left-hand column: time evolution of the v_y component (solid line) of the velocity vector at the first receiver (located not too far from the source and close to the opposite PML layer) with CPML using $\alpha_{\max} = \pi f_0$ and $\kappa_{\max} = 1$ compared to a reference solution (medium dashed) computed in a much larger domain for the numerical experiment of Fig. 1. The dotted lines represent the difference multiplied by a factor of 10 in order to visualize small errors that would otherwise not be clearly visible. At this receiver located close to the PML layer, very small discrepancies are observed between all curves (including the difference between seismograms with and without frequency shift) for values of $\kappa_{\max} = 7$ or 20 (not shown here), that is, making κ_{\max} increase from 1 to 20 does not significantly change the solution. This illustrates the good efficiency of the CPML for all values of κ_{\max} . Right-hand panel: same comparison when CPML with no shift of the poles in the stretching function (i.e. $\alpha_{\max} = 0$) is used in the numerical experiment of Fig. 2. For all values of κ_{\max} , the results are very similar to the CPML result obtained with frequency shift.

In the non-shifted case, amplitudes are slightly improved using $\kappa_{\max} = 7$ or 20 compared with $\kappa_{\max} = 1$.

In summary, the functions κ_i help to improve the solution in terms of phase and amplitude as can be observed in all the seismograms. However, κ_{\max} should not be increased too much because the limited number of points in the damping direction of each PML region cannot accurately sample large and rapid variations of the κ_i functions.

4.3 Energy decay with CPML

Let us study the decay of total energy in the mesh in order to analyse more precisely the efficiency of the CPML, including at grazing incidence. After some algebraic manipulations of the equations we have

$$\begin{aligned} \frac{1}{2} \frac{d}{dt} \left[\int_{\Omega} \rho \|\mathbf{v}\|^2 + \mathbf{T}^R : \boldsymbol{\varepsilon} + \sum_{l=1}^L \tau_{\sigma l} (\delta \mathbf{c}^l)^{-1} \mathbf{R}^l : \mathbf{R}^l d\Omega \right] \\ = - \sum_{l=1}^L \int_{\Omega} \tau_{\sigma l}^2 (\delta \mathbf{c}^l)^{-1} \frac{d\mathbf{R}^l}{dt} : \frac{d\mathbf{R}^l}{dt} d\Omega, \end{aligned} \quad (30)$$

where \mathbf{T}^R is the relaxed stress tensor. Using the fact that the tensor $\delta \mathbf{c}^l$ is strictly positive definite, the quantity

$$E = \frac{1}{2} \int_{\Omega} \rho \|\mathbf{v}\|^2 + \mathbf{T}^R : \boldsymbol{\varepsilon} + \sum_{l=1}^L \tau_{\sigma l} (\delta \mathbf{c}^l)^{-1} \mathbf{R}^l : \mathbf{R}^l d\Omega \quad (31)$$

is positive and represents an energy. In Fig. 6, we represent the time decay of that total energy E in the inner part of the model (i.e. in the medium without the six CPML layers) for $\alpha_{\max} = 0$ and πf_0 and increasing values of κ_{\max} for the simulation presented in Fig. 1, and we summarize the measurements in Table 2. We compare the evolution of total energy over 14 500 steps (5.075 s) and a longer time period of 100 000 steps (35 s) using non-shifted and shifted CPML to experimentally test the numerical stability of CPML, because it is known that in numerous PML models, for instance in the case of Maxwell's equations, weak or strong instabilities can develop for long simulations (Abarbanel *et al.* 2002; Bécache & Joly 2002; Bécache *et al.* 2004).

In all these simulations, the source injects energy into the system for approximately 0.15 s. Then the energy carried by the direct,

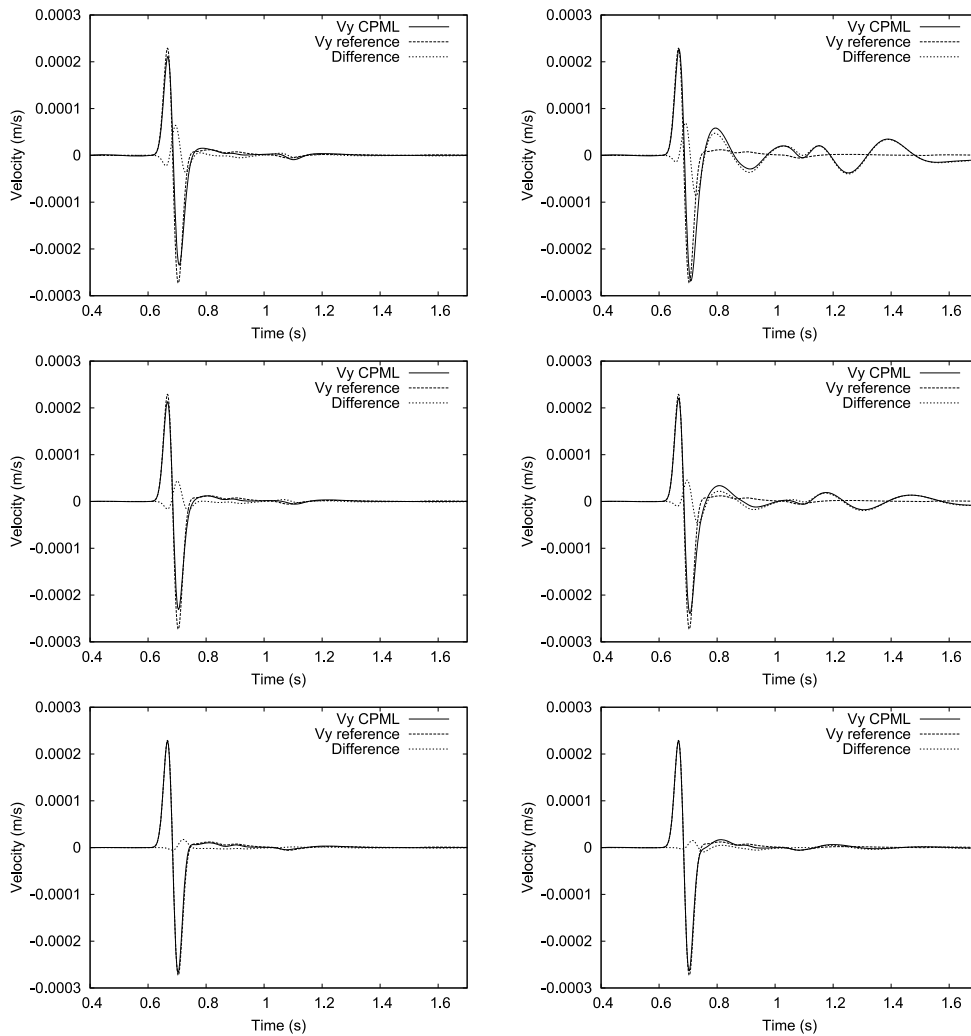


Figure 4. Left-hand column: time evolution of the v_y component (solid line) of the velocity vector with CPML with $\alpha_{\max} = \pi f_0$ and $\kappa_{\max} = 1$ (top panel), 7 (middle panel) or 20 (bottom panel) at the second receiver located close to the left PML in the upper layer compared to a reference solution (medium dashed) computed in a much larger domain with no absorbing conditions for the numerical experiment of Fig. 1. The dotted line represents the difference. At this receiver located close to the PML layer, some small discrepancies are observed between the two curves for a value of $\kappa_{\max} = 1$, but they become less important when κ_{\max} is increased to 20. This illustrates the good efficiency of the CPML at large offset and close to the base of the PML when a frequency shift is introduced and when high values of κ_{\max} are used. Right-hand column: same comparison when CPML with no shift of the poles in the stretching function (i.e. $\alpha_{\max} = 0$) is used in the numerical experiment of Fig. 2. At grazing incidence large spurious oscillations develop and the pressure and shear waves are significantly distorted. A value of $\kappa_{\max} = 20$ gives slightly better results than 1 or 7.

reflected and transmitted pressure waves and shear waves is gradually absorbed by the CPML layers, and after approximately 2 s all waves should have disappeared and there should remain no energy in the medium. All the remaining energy is therefore spurious and is a good measurement of the efficiency of the absorbing boundary layer. For simulations performed with $\alpha_{\max} = 0$, at 2 s a total energy of 8.86 J remains in the case of $\kappa_{\max} = 1$, while for $\kappa_{\max} = 7$ or 20 the value of energy is, respectively, 1.875 and 0.1 J (i.e. a factor of 4.72 or 88.6 smaller). Then, at 5 s, total energy decreases to a value of 1.36×10^{-3} J for $\kappa_{\max} = 1$, and to values of 1.4×10^{-3} and 9.93×10^{-4} J for $\kappa_{\max} = 7$ and 20, that is, factors of 0.97 or 1.37 smaller. Then, for medium (14 s) and longer (35 s) time periods total energy reaches very similar values, respectively, in the range of 1.12×10^{-7} to 1.24×10^{-7} J and 1.27×10^{-10} to 1.3×10^{-10} J for the different values of κ_{\max} considered.

In the case of the shifted CPML for $\alpha_{\max} = \pi f_0$ (Fig. 6), total energy is smaller than in the case of $\alpha_{\max} = 0$ presented above. At

2 s, similar values of total energy of 3.52×10^{-4} , 2.33×10^{-4} and 3.18×10^{-4} J remain in the respective cases of shifted CPML with $\kappa_{\max} = 1$, 7 or 20 (i.e. a factor of 25 170, 8046 or 314 smaller compared to $\alpha_{\max} = 0$). At 5 s, total energy decreases to values of 3.96×10^{-5} , 2.82×10^{-5} and 4.16×10^{-5} J, respectively for $\kappa_{\max} = 1$, 7 or 20, that is, a factor of 34, 50 or 24 smaller. Then, for a medium time period (14 s), energy reaches closer values of 5.32×10^{-10} , 1.72×10^{-10} or 5.19×10^{-10} J for $\kappa_{\max} = 1$, 7 or 20, respectively.

To experimentally analyse long time stability from a numerical point of view, in Fig. 6 we also show the evolution of total energy over 35 s (i.e. 100 000 time steps) in the case of the shifted CPML for the experiments of Figs 1 and 2. It decreases very rapidly and non-linearly and no instabilities are observed on this semi-logarithmic curve, which means that the discrete CPML is stable up to 100 000 time steps, reaching final values of 4.44×10^{-22} , 5.34×10^{-23} or 2.78×10^{-22} J, respectively for $\kappa_{\max} = 1$, 7 or 20,

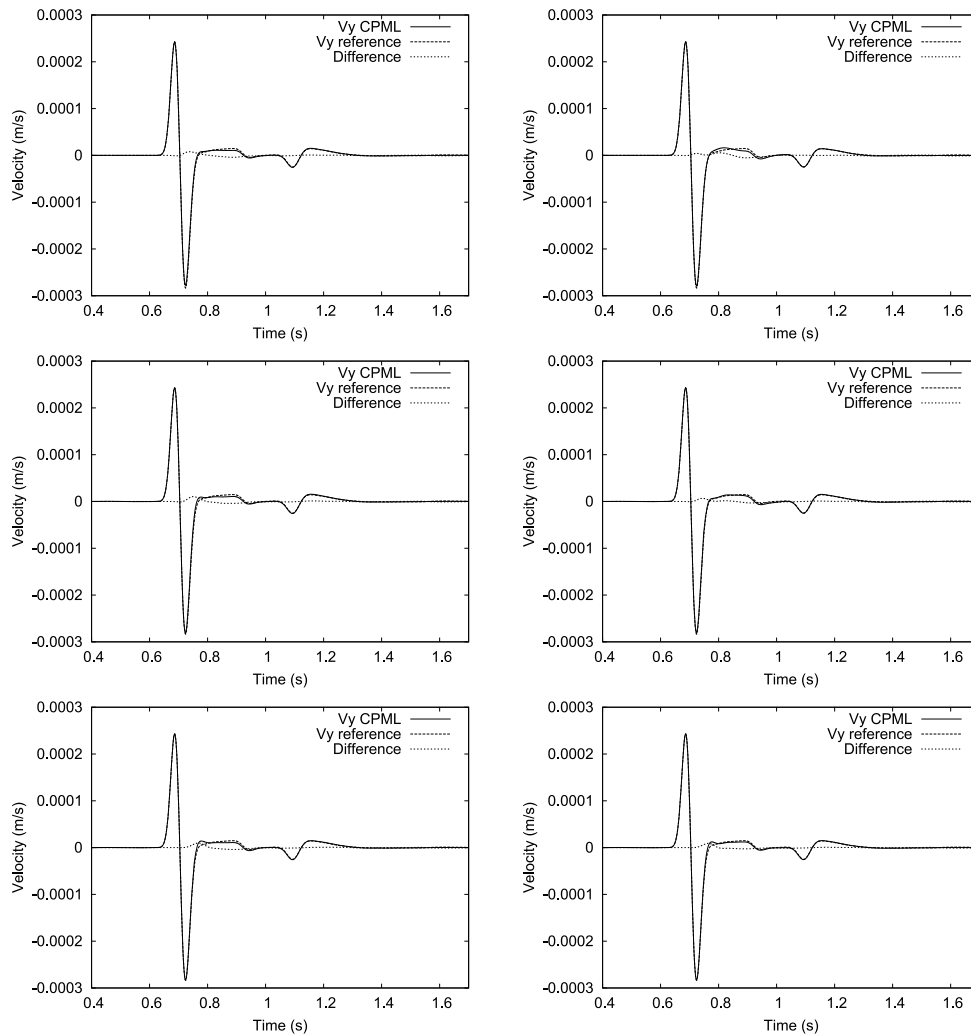


Figure 5. Left-hand column: time evolution of the v_y component (solid line) of the velocity vector with CPML using $\alpha_{\max} = \pi f_0$ and $\kappa_{\max} = 1$ (top panel), 7 (middle panel) or 20 (bottom panel) at the third receiver located in the upper layer close to the right PML compared to a reference solution (medium dashed) computed in a much larger domain with no absorbing condition for the numerical experiment of Fig. 1. The dotted line represents the difference. At this receiver located close to the PML layer, some discrepancies are observed between the two curves for values of $\kappa_{\max} = 1$, but they become less important when κ_{\max} is increased to 20. This illustrates the good efficiency of the CPML when a frequency shift is introduced and for large values of κ_{\max} . Right-hand column: same comparison when CPML with no shift of the poles in the stretching function (i.e. $\alpha_{\max} = 0$) is used in the numerical experiment of Fig. 2. At grazing incidence small spurious oscillations appear and the pressure and shear waves are distorted, but less than at the second receiver located at grazing incidence and vertically above the source. A value of $\kappa_{\max} = 20$ gives slightly better results than 1 or 7.

while total energy reaches a much higher value of around 1.3×10^{-10} J in the non-shifted CPML case as mentioned above. Very large total energy reduction factors of 3.4×10^{12} , 4.1×10^{13} and 2.1×10^{12} are therefore obtained for $\alpha_{\max} = \pi f_0$ and $\kappa_{\max} = 1, 7$ or 20.

It is worth mentioning that weak oscillations appear at medium and long times in spite of the fact that total energy decays very quickly in average. This illustrates the fact that re-injections of energy in the main domain and damping phenomena occur at long time periods beyond approximately 4 s due to the introduction of the variables α_i that improve the solution at grazing incidence and also at large offset (i.e. at points located far from the source) at the expense of the generation of a small amount of low frequency energy reflected off the CPML regions and coming back into the main domain. This has also been observed for PML applied to Maxwell's equations.

5 CONCLUSIONS

We have introduced an unsplit CPML boundary condition for the viscoelastic seismic wave equation that is particularly useful when two or more SLS mechanisms are used (which is always the case in practice; usually three or more are used). This method is well suited for waves impinging the boundary at grazing incidence. For only one mechanism, this CPML has approximately the same memory storage as the classical PML but absorbs waves at grazing incidence much better than PML. Memory storage is reduced by 40 per cent in the PML regions compared to the split GFPML of Festa & Vilotte (2005) and by more than 70 per cent when two mechanisms are used.

Furthermore, the attenuation mechanism time-marching equations do not need to be split. As a consequence, in these mechanism equations only the modified gradient of the velocities and its CPML

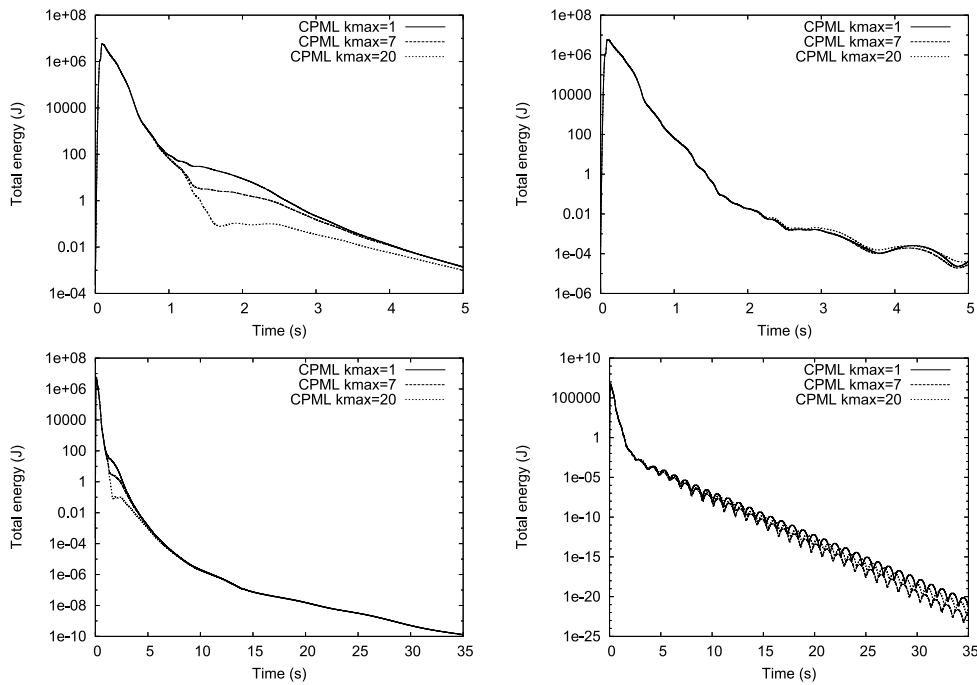


Figure 6. Left-hand panel: decay of total energy with time in the main domain (i.e. without the six PML layers) for medium (5 s, top panel) and longer (35 s, bottom panel) time periods on a semi-logarithmic scale for the simulations of Figs 1 and 2. Solid, long dashed and medium dashed lines correspond to CPML for $\alpha_{\max} = 0$ and $\kappa_{\max} = 1, 7$ or 20 , respectively. Right-hand panel: same curves as in the left-hand column but for $\alpha_{\max} = \pi f_0$. To study the stability of the shifted CPML at longer times, we make the experiment of Fig. 1 last for 100 000 time steps (i.e. 35 s, bottom panel). The amount of spurious total energy that remains in the mesh decreases continuously and reaches values as low as 4.44×10^{-22} , 5.34×10^{-23} or 2.78×10^{-22} J, respectively for $\kappa_{\max} = 1, 7$ and 20 . No instabilities are observed on this semi-logarithmic scale, which means that the discrete CPML is stable up to 100 000 steps. Spurious total energy is smaller by 12–13 orders of magnitude for the shifted CPML compared to the non-shifted CPML.

Table 2. Value of total energy (in Joules) in the mesh when CPML is implemented for two values of α_{\max} (0 or πf_0) and κ_{\max} ($1, 7$ or 20) at different times (2, 5, 14 and 35 s). Using $\alpha_{\max} = \pi f_0$ the spurious total energy remaining in the mesh is drastically reduced by 2 to 3 orders of magnitude in the first few seconds of the simulation and by 12–13 orders of magnitude after a longer time period of 35 s.

Time	2 s	5 s	14 s	35 s
$\alpha_{\max} = 0, \kappa_{\max} = 1$	8.86	1.36×10^{-3}	1.24×10^{-7}	1.3×10^{-10}
$\alpha_{\max} = 0, \kappa_{\max} = 7$	1.875	1.4×10^{-3}	1.14×10^{-7}	1.28×10^{-10}
$\alpha_{\max} = 0, \kappa_{\max} = 20$	0.1	9.93×10^{-4}	1.12×10^{-7}	1.27×10^{-10}
$\alpha_{\max} = \pi f_0, \kappa_{\max} = 1$	3.52×10^{-4}	3.96×10^{-5}	5.32×10^{-10}	4.44×10^{-22}
$\alpha_{\max} = \pi f_0, \kappa_{\max} = 7$	2.33×10^{-4}	2.82×10^{-5}	1.72×10^{-10}	5.34×10^{-23}
$\alpha_{\max} = \pi f_0, \kappa_{\max} = 20$	3.18×10^{-4}	4.16×10^{-5}	5.19×10^{-10}	2.78×10^{-22}

auxiliary variable need to be computed once at each time step, which further reduces memory storage in the PML regions compared to the classical split PML or split GFPML.

Experimentally, stability is ensured for 100 000 time steps, and reduction factors up to 13 orders of magnitude are obtained in terms of remaining spurious total energy. Increasing the values of κ_{\max} from 1 to 20 increases the accuracy of the calculations for both the shifted and non-shifted CPML.

ACKNOWLEDGMENTS

The authors thank Stephen D. Gedney for fruitful discussions and for providing them with his CPML software package for Maxwell's equations. They also thank two anonymous reviewers and the associate editor for comments that improved the manuscript. Calculations were performed at IDRIS in Orsay and CINES/GENCI in Montpellier (France).

REFERENCES

- Abarbanel, S., Gottlieb, D. & Hesthaven, J.S., 2002. Long time behavior of the perfectly matched layer equations in computational electromagnetics, *J. Scient. Comput.*, **17**(1–4), 405–422.
- Bécache, E. & Joly, P., 2002. On the analysis of Bérenger's perfectly matched layers for Maxwell's equations, *Math. Modell. Numer. Anal.*, **36**(1), 87–120.
- Bécache, E., Petropoulos, P.G. & Gedney, S.G., 2004. On the long-time behavior of unsplit perfectly matched layers, *IEEE Trans. Antennas Propag.*, **52**(5), 1335–1342.
- Bérenger, J.P., 1994. A perfectly matched layer for the absorption of electromagnetic waves, *J. Comput. Phys.*, **114**, 185–200.
- Carcione, J.M., 1993. Seismic modeling in viscoelastic media, *Geophysics*, **58**(1), 110–120.
- Carcione, J.M., 2007. *Wave Fields in Real Media: Theory and Numerical Simulation of Wave Propagation in Anisotropic, Anelastic, Porous and Electromagnetic Media*, 2nd edn, Elsevier Science, Amsterdam, The Netherlands.

- Carcione, J.M., Kosloff, D. & Kosloff, R., 1988. Wave propagation simulation in a linear viscoelastic medium, *Geophys. J. Int.*, **95**, 597–611.
- Cerjan, C., Kosloff, D., Kosloff, R. & Reshef, M., 1985. A nonreflecting boundary condition for discrete acoustic and elastic wave equation, *Geophysics*, **50**, 705–708.
- Chew, W.C. & Liu, Q., 1996. Perfectly matched layers for elastodynamics: a new absorbing boundary condition, *J. Comput. Acoust.*, **4**(4), 341–359.
- Chew, W.C. & Weedon, W.H., 1994. A 3-D perfectly matched medium from modified Maxwell's equations with stretched coordinates, *Microw. Opt. Technol. Lett.*, **7**(13), 599–604.
- Clayton, R. & Engquist, B., 1977. Absorbing boundary conditions for acoustic and elastic wave equations, *Bull. seism. Soc. Am.*, **67**, 1529–1540.
- Cohen, G. & Fauquaux, S., 2005. Mixed spectral finite elements for the linear elasticity system in unbounded domains, *SIAM J. Scient. Comput.*, **26**(3), 864–884.
- Collino, F. & Monk, P., 1998. The perfectly matched layer in curvilinear coordinates, *SIAM J. Sci. Comput.*, **19**(6), 2061–2090.
- Collino, F. & Tsogka, C., 2001. Application of the PML absorbing layer model to the linear elastodynamic problem in anisotropic heterogeneous media, *Geophysics*, **66**(1), 294–307.
- Courant, R., Friedrichs, K.O. & Lewy, H., 1928. Über die partiellen Differenzengleichungen der mathematischen Physik, *Mathematische Annalen*, **100**, 32–74.
- Dong, L., She, D., Guan, L. & Ma, Z., 2005. An eigenvalue decomposition method to construct absorbing boundary conditions for acoustic and elastic wave equations, *J. geophys. Eng.*, **2**, 192–198.
- Drossaert, F.H. & Giannopoulos, A., 2007. A nonsplit complex frequency-shifted PML based on recursive integration for FDTD modeling of elastic waves, *Geophysics*, **72**(2), T9–T17.
- Emmerich, H. & Korn, M., 1987. Incorporation of attenuation into time-domain computations of seismic wave fields, *Geophysics*, **52**, 1252–1264.
- Engquist, B. & Majda, A., 1977. Absorbing boundary conditions for the numerical simulation of waves, *Math. Comp.*, **31**, 629–651.
- Festa, G. & Vilotte, J.P., 2005. The Newmark scheme as velocity-stress time-staggering: an efficient PML implementation for spectral-element simulations of elastodynamics, *Geophys. J. Int.*, **161**, 789–812.
- Festa, G., Delavaud, E. & Vilotte, J.P., 2005. Interaction between surface waves and absorbing boundaries for wave propagation in geological basins: 2D numerical simulations, *Geophys. Res. Lett.*, **32**(20), L20306, doi:10.1029/2005GL024091.
- Gedney, S.D., 1998. The Perfectly Matched Layer absorbing medium, in *Advances in Computational Electrodynamics: the Finite-Difference Time-Domain Method*, Chap. 5, pp. 263–343, ed. Taflov, A., Artech House, Boston, USA.
- Givoli, D., 1991. Non-reflecting boundary conditions: review article, *J. Comput. Phys.*, **94**, 1–29.
- Grote, M.J., 2000. Nonreflecting boundary conditions for elastodynamics scattering, *J. Comput. Phys.*, **161**, 331–353.
- Guddati, M.N. & Lim, K.W., 2006. Continued fraction absorbing boundary conditions for convex polygonal domains, *Int. J. Numer. Meth. Eng.*, **66**(6), 949–977.
- Hagstrom, T. & Hariharan, S.I., 1998. A formulation of asymptotic and exact boundary conditions using local operators, *Appl. Num. Math.*, **27**, 403–416.
- Higdon, R.L., 1991. Absorbing boundary conditions for elastic waves, *Geophysics*, **56**, 231–241.
- Komatitsch, D. & Martin, R., 2007. An unsplit convolutional perfectly matched layer improved at grazing incidence for the seismic wave equation, *Geophysics*, **72**(5), SM155–SM167.
- Komatitsch, D. & Tromp, J., 1999. Introduction to the spectral-element method for 3-D seismic wave propagation, *Geophys. J. Int.*, **139**(3), 806–822.
- Komatitsch, D. & Tromp, J., 2003. A perfectly matched layer absorbing boundary condition for the second-order seismic wave equation, *Geophys. J. Int.*, **154**(1), 146–153.
- Liu, H.P., Anderson, D.L. & Kanamori, H., 1976. Velocity dispersion due to anelasticity: implications for seismology and mantle composition, *Geophys. J. R. astr. Soc.*, **47**, 41–58.
- Luebbers, R.J. & Hunsberger, F., 1992. FDTD for Nth-order dispersive media, *IEEE Trans. Antennas Propag.*, **40**(11), 1297–1301.
- Ma, S. & Liu, P., 2006. Modeling of the perfectly matched layer absorbing boundaries and intrinsic attenuation in explicit finite-element methods, *Bull. seism. Soc. Am.*, **96**(5), 1779–1794.
- Martin, R., Komatitsch, D. & Ezziani, A., 2008a. An unsplit convolutional perfectly matched layer improved at grazing incidence for seismic wave equation in poroelastic media, *Geophysics*, **73**(4), T51–T61.
- Martin, R., Komatitsch, D. & Gedney, S.D., 2008b. A variational formulation of a stabilized unsplit convolutional perfectly matched layer for the isotropic or anisotropic seismic wave equation, *Comput. Modell. Eng. Sci.*, **37**(3), 274–304.
- Moczo, P. & Kristek, J., 2005. On the rheological models used for time-domain methods of seismic wave propagation, *Geophys. Res. Lett.*, **32**, L01306.
- Moczo, P., Robertsson, J. & Eisner, L., 2007. The finite-difference time-domain method for modeling of seismic wave propagation, in *Advances in Wave Propagation in Heterogeneous Media*, Vol. 48 chap. 8, pp. 421–516, eds Wu, R.-S. & Maupin, V., Advances in Geophysics, Elsevier – Academic Press.
- Peng, C.B. & Tökösz, M.N., 1995. An optimal absorbing boundary condition for elastic wave modeling, *Geophysics*, **60**, 296–301.
- Quarteroni, A., Tagliani, A. & Zampieri, E., 1998. Generalized Galerkin approximations of elastic waves with absorbing boundary conditions, *Comput. Meth. appl. Mech. Eng.*, **163**, 323–341.
- Roden, J.A. & Gedney, S.D., 2000. Convolution PML (CPML): an efficient FDTD implementation of the CFS-PML for arbitrary media, *Microw. Opt. Technol. Lett.*, **27**(5), 334–339.
- Sochacki, J., Kubicek, R., George, J., Fletcher, W.R. & Smithson, S., 1987. Absorbing boundary conditions and surface waves, *Geophysics*, **52**(1), 60–71.
- Stacey, R., 1988. Improved transparent boundary formulations for the elastic wave equation, *Bull. seism. Soc. Am.*, **78**(6), 2089–2097.
- Zeng, Y.Q., He, J.Q. & Liu, Q.H., 2001. The application of the perfectly matched layer in numerical modeling of wave propagation in poroelastic media, *Geophysics*, **66**(4), 1258–1266.

APPENDIX: THE VELOCITY-FORMULATION OF THE VISCOELASTIC WAVE EQUATION

Detailed expressions of the velocity–stress formulation of the viscoelastic wave equation using SLS relaxation mechanisms are given for instance in Carcione (1993). Using the same notations and developing eq. (12) one gets

$$\partial_t \rho v_x = \partial_x T_{xx} + \partial_y T_{xy} + \partial_z T_{xz}$$

$$\partial_t \rho v_y = \partial_x T_{xy} + \partial_y T_{yy} + \partial_z T_{yz}$$

$$\partial_t \rho v_z = \partial_x T_{xz} + \partial_y T_{yz} + \partial_z T_{zz}$$

$$\partial_t T_{xy} = \mu^U (\partial_y v_x + \partial_x v_y) + \sum_{\ell=1}^L \mathbf{R}_{xy}^{\ell}$$

$$\partial_t T_{xz} = \mu^U (\partial_z v_x + \partial_x v_z) + \sum_{\ell=1}^L \mathbf{R}_{xz}^{\ell}$$

$$\partial_t T_{yz} = \mu^U (\partial_z v_y + \partial_y v_z) + \sum_{\ell=1}^L \mathbf{R}_{yz}^{\ell}$$

$$\partial_t T_{xx} = (\lambda^U + 2\mu^U) \partial_x v_x + \lambda^U (\partial_y v_y + \partial_z v_z) + \sum_{\ell=1}^L \mathbf{R}_{xx}^{\ell}$$

$$\partial_t T_{yy} = \lambda^U (\partial_x v_x + \partial_z v_z) + (\lambda^U + 2\mu^U) \partial_y v_y + \sum_{\ell=1}^L \mathbf{R}_{yy}^{\ell}$$

$$\begin{aligned}
 \partial_t T_{zz} &= \lambda^U (\partial_x v_x + \partial_y v_y) + (\lambda^U + 2\mu^U) \partial_z v_z + \sum_{\ell=1}^L \mathbf{R}_{zz}^\ell \\
 \partial_t \mathbf{E}_1^\ell &= -\mathbf{E}_1^\ell / \tau_{\sigma\ell}^1 + \Theta \phi_{1\ell} \\
 \partial_t \mathbf{E}_{11}^\ell &= -\mathbf{E}_{11}^\ell / \tau_{\sigma\ell}^2 + \left(\partial_x v_x - \frac{\Theta}{D} \right) \phi_{2\ell} \\
 \partial_t \mathbf{E}_{22}^\ell &= -\mathbf{E}_{22}^\ell / \tau_{\sigma\ell}^2 + \left(\partial_y v_y - \frac{\Theta}{D} \right) \phi_{2\ell} \\
 \partial_t \mathbf{E}_{12}^\ell &= -\mathbf{E}_{12}^\ell / \tau_{\sigma\ell}^2 + (\partial_y v_x + \partial_x v_y) \phi_{2\ell} \\
 \partial_t \mathbf{E}_{13}^\ell &= -\mathbf{E}_{13}^\ell / \tau_{\sigma\ell}^2 + (\partial_z v_x + \partial_x v_z) \phi_{2\ell} \\
 \partial_t \mathbf{E}_{23}^\ell &= -\mathbf{E}_{23}^\ell / \tau_{\sigma\ell}^2 + (\partial_z v_y + \partial_y v_z) \phi_{2\ell},
 \end{aligned} \tag{A1}$$

where

$$\Theta = \partial_x v_x + \partial_y v_y + \partial_z v_z \tag{A2}$$

is the compressional component of the wave field,

$$\lambda^U = (\lambda^R + 2\mu^R) M^{U1} - \frac{2}{D} \mu^R M^{U2}$$

$$\mu^U = \mu^R M^{U2}$$

$$\phi_{vl} = \left(1 - \frac{\tau_{\epsilon l}^v}{\tau_{\sigma l}^v} \right) / \tau_{\sigma l}^v \tag{A3}$$

are the unrelaxed (i.e. high frequency) Lamé parameters and $M^{U\nu}$, $\nu = 1, 2$, are the relaxation functions, where $\nu = 1$ is the compressional mode and $\nu = 2$ is the shear mode. The expression of $M^{U\nu}$, $\nu = 1, 2$ is

$$M^{U\nu} = 1 - \sum_{\ell=1}^{L\nu} \left(1 - \frac{\tau_{\epsilon l}^v}{\tau_{\sigma l}^v} \right), \nu = 1, 2 \tag{A4}$$

where $\tau_{\epsilon l}^v$ and $\tau_{\sigma l}^v$ are given relaxation times. The L_1 memory variables e_{1l} correspond to the L_1 standard mechanisms that describe the anelastic compressional wave while the memory variables e_{11l} , e_{22l} , e_{12l} , e_{13l} , e_{23l} correspond to the L_2 mechanisms of the shear wave.

The solid mechanisms \mathbf{R}_{mn}^ℓ can be expressed as a combination of elemental mechanisms \mathbf{E}_{ij}^ℓ

$$\begin{aligned}
 \mathbf{R}_{xx}^\ell &= (\lambda^R + 2\mu^R / D) (\mathbf{E}_1^\ell + 2\mu^R \mathbf{E}_{11}^\ell) \\
 \mathbf{R}_{yy}^\ell &= (\lambda^R + 2\mu^R / D) (\mathbf{E}_1^\ell + 2\mu^R \mathbf{E}_{22}^\ell) \\
 \mathbf{R}_{zz}^\ell &= (\lambda^R + 2\mu^R) \mathbf{E}_1^\ell - \frac{2}{D} \mu^R (\mathbf{E}_{11}^\ell + \mathbf{E}_{22}^\ell) \\
 \mathbf{R}_{xy}^\ell &= \mu^R \mathbf{E}_{12}^\ell \\
 \mathbf{R}_{xz}^\ell &= \mu^R \mathbf{E}_{13}^\ell \\
 \mathbf{R}_{yz}^\ell &= \mu^R \mathbf{E}_{23}^\ell.
 \end{aligned} \tag{A5}$$